Journal of
Micro/Nanolithography,
MEMS, and MOEMS

Nanolithography.SPIEDigitalLibrary.org

Localized and cascading secondary electron generation as causes of stochastic defects in extreme ultraviolet projection lithography

Hiroshi Fukuda

SPIE.

Hiroshi Fukuda, "Localized and cascading secondary electron generation as causes of stochastic defects in extreme ultraviolet projection lithography," *J. Micro/Nanolith. MEMS MOEMS* **18**(1), 013503 (2019), doi: 10.1117/1.JMM.18.1.013503.

Localized and cascading secondary electron generation as causes of stochastic defects in extreme ultraviolet projection lithography

Hiroshi Fukuda*
Hitachi High-Technologies Corporation, Tokyo, Japan

Abstract. Projection lithography using extreme ultraviolet (EUV) light at 13-nm wavelength is expected to achieve production of integrated circuits below 10 nm design-rules. In pursuit of further miniaturization, however, stochastic pattern defect problems have arisen. Here, we discuss the possible impact of spatially inhomogeneous secondary electron (SE) generation on stochastic defects. Two mechanisms are investigated: (1) accidental connections of photon shot noises enhanced by densely localized SE generation and (2) cascading SE generation along photoelectron trajectory traveling from pattern edge into a dark region. Since such defect probabilities are extremely low (typically 10^{-4} to $\sim 10^{-12}$), results of Monte Carlo simulation based on classical optical image and electron scattering simulations are converted into probability functions for densities of physical/chemical events such as photon absorption, SE generation, and elementary reaction in chemically amplified resists. Probabilities of pattern formation and of defect generation are modeled using these functions. Results of performance optimization using a multiobjective genetic algorithm show higher stochastic defects probability in EUV than in conventional deep-UV exposure due to larger spatial inhomogeneity in reaction density and existence of SE generation strings. Defect probabilities are strongly dependent on absolute pattern sizes in the two mechanisms, regardless of the resolution capability of imaging systems. Guidelines for suppressing stochastic defects are suggested, such as homogenization of reaction density, material composition for increasing scattering cross-section, and suppression of pattern edge fluctuation. [DOI: 10.1117/1.JMM.18.1.013503]

Keywords: lithography; extreme ultraviolet; chemically amplified resists; stochastic defect; secondary electron; Monte Carlo simulation.

Paper 18140 received Nov. 20, 2018; accepted for publication Jan. 15, 2019; published online Feb. 8, 2019; corrected Jul. 13, 2022.

1 Introduction

In pursuit of further miniaturization of semiconductor integrated circuit devices by projection lithography using extreme ultraviolet (EUV) light at 13-nm wavelength, stochastic pattern defect problems have arisen.[1–3] As the feature size of circuit patterns (~10 nm) is approaching to the size of resist molecule/polymer (1 to 2 nm), nanometer level roughness on pattern edges (often called line edge roughness, LER) becomes a problem.[4,5] In contrast, the stochastic defects are fatal patterning failures such as bridging between neighboring lines or breakages of lines. The probability of such defect generations heavily depends on pattern feature sizes[1] and span in a wide range (10^{-12} to 10^{-4}). Because cutting-edge integrated circuit devices today have more than 10^{12} critical features per device layer on a 300-mm wafer, such a defect probability will result in an unacceptable level of defect density. Because no such problem has been reported for conventional deep UV (DUV) lithography using ArF excimer laser light (193 nm), they are material problems appearing in regime only below 40 nm or problems caused by the differences in exposure wavelength. Differences in photon energy can affect patterning performances through two aspects, photon number density and reaction mechanism.[6–9] This paper discusses cascading shot noises and long-range scattered photoelectrons as causes of these stochastic defects. Since such defect probability is extremely low, we need to introduce probabilistic approaches into patterning analyses based on physics and chemistry. Although a typical approach to this is the Monte Carlo method, capturing such an extremely low probability phenomenon requires huge calculation time and resources. In this study, we describe systems by combinations of subsystems and build probabilistic models for each subsystem using Monte Carlo method. This enables us to calculate an extremely low probability as a product of moderately low probabilities and to keep calculation size within an acceptable range.

2 Statistical Model of Resist Reactions

First, we start from generating physical events using Monte Carlo simulations as follows. Atoms or chemical bonds in resist materials absorb photon energy at random position inside resist films with a probability proportional to optical image intensity. Here, we calculate horizontal image intensity distribution on resist film surface simply using Hopkins theory and apply Lambert Beer's law to obtain distribution inside resist films.[10] For EUV exposure, atoms emit photoelectrons in random directions upon photon absorption. Photoelectrons change their directions by elastic scattering, lose their energies by inelastic scattering with generating secondary electrons (SE), and stop when their energies become lower than a certain threshold level. The discrete loss approximation is used in modeling electron scattering

*Address all correspondence to Hiroshi Fukuda, E-mail: hiroshi.fukuda.zp@hitachi-hightech.com

processes since cross-sections for elastic and inelastic scattering are comparable for the low energy range of photoelectron produced by EUV.[11–12]

We assume two types of resist materials: chemically amplified resists (CAR) and nonchemically amplified metal-containing resists, such as metal oxide materials (MOx). In CAR,[13–16] photoacid generator molecules generate photoacid upon absorbing photon energy for DUV exposure or SE energy for EUV exposures.[17] Here, we include the discrepancies between the locations of acid generation and photon absorption/SE generation in randomness of photon absorption or SE generation as approximation. Acids promote acid-catalytic reactions to flip the polarity of polar moieties in resist matrix polymers or molecules within the diffusion range of acid. A matrix polymer/molecule contains several polar moieties and changes its solubility when the number of polarity flip exceeds a certain threshold. The average number of polarity flipping reactions per acid is limited to catalytic chain length due to acid life-time or reaction site number within diffusion ranges. The probability of acid-catalytic reaction is in proportion to acid existence probability, which is approximated by Gaussian distribution centered at acid generation site with acid diffusion length as a blur. In contrast, MOx contains metallic composites to enhance EUV photon absorption.[18] The elementary reaction to flip the solubility of the molecule takes place somewhere in proportion to SE existence probability, which is approximated by Gaussian distribution centered at SE generation site with SE mean-free-path as a blur. We omit the nanoscale inhomogeneity in resist compositions in this study.[19]

To visualize the above-reaction mechanisms, Fig. 1 shows the simulated distributions of photon absorptions (red spheres), SE generations (blue spheres, for EUV), and elementary reactions (green spheres) for three typical material systems, DUV exposed CAR, EUV exposed MOx, and EUV exposed CAR. For purely comparing material systems, the same irradiation dosage (20 $\mathrm{mJ/cm^2}$) and optical image distribution (16 nm lines and spaces by EUV, NA0.33 equivalent) are hypothetically assumed. For the same dosage, the area density of photon number in EUV is 1/15th of that in ArF.

For ArF resists with photoabsorption $\alpha = 0.001$ and 0.004 $\mathrm{nm^{-1}}$, the averaged distances between photon absorption sites inside resist $d_{\text{inter-PA}}$, defined by (volumetric photon absorption density)$^{1/3}$ are 1.7 and 1.1 nm at 20 $\mathrm{mJ/cm^2}$, respectively. Reactions in the space among photon absorption sites need to be promoted by acid diffusion, and an acid-diffusion length is required to cover this range. For EUV/MOx, $\alpha = 0.02$ $\mathrm{nm^{-1}}$ is reported, and $d_{\text{inter-PA}}$ is 1.7 nm at 20 $\mathrm{mJ/cm^2}$. Reactions in the space among photon absorption sites are filled by plural SEs generated along photoelectron trajectories. Here, note a wide variety in the spatial distributions of generated SE; sometimes they are highly localized while sometimes they extend asymmetrically along long trajectories of photoelectrons.

In EUV/CAR, photon-absorption is sparser than in MOx due to moderate photoabsorption ($d_{\text{inter-PA}} = 2.5$ nm at 20 $\mathrm{mJ/cm^2}$ for $\alpha = 0.005$ $\mathrm{nm^{-1}}$). In addition to SE generations along photoelectron trajectories, acid diffusion homogenizes reaction site distributions around each SE.

Next, to apply statistical analyses to the results of the above Monte Carlo simulations, we divide resist films

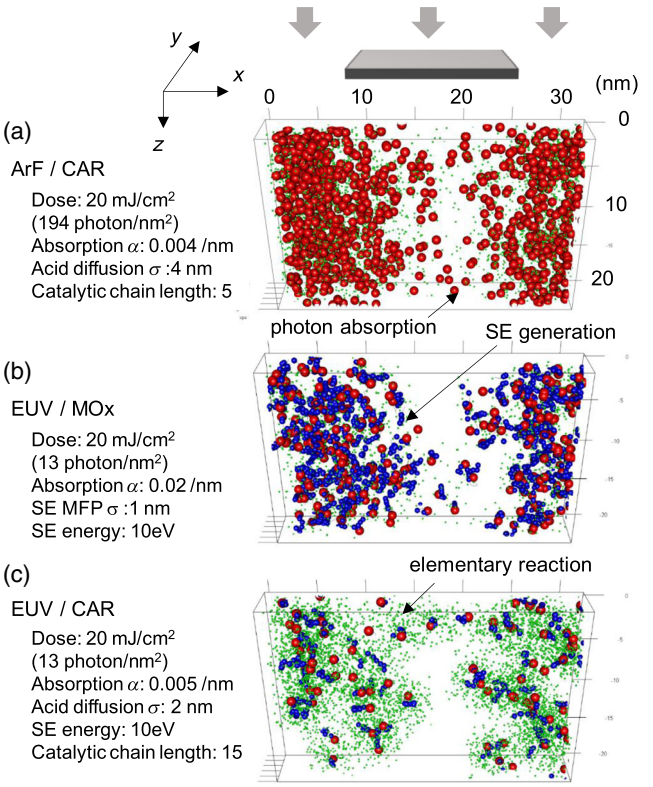

Fig. 1 Simulated distributions of photon absorptions (red spheres), SE generations (blue spheres, for EUV), and acid-catalytic reactions (green spheres, for CAR) for (a) DUV exposed CAR, (b) EUV exposed MOx, and (c) EUV exposed CAR. For purely comparing material systems, the same optical image distribution (16 nm lines and spaces by EUV, NA0.33 equivalent) is assumed.

into small segments using three-dimensional (3-D) grids (typically 1 nm step size in this study) and introduce voxel defined as a cube with 1 nm side in x, y, and z dimensions as the approximation of minimum soluble units such as resist polymers or molecules. Here, we assume one-dimensional (1-D) periodic patterns with image modulated in the x-direction. The centers of the exposed area, the edge, and the center of the masked area are located at $x = 0$, pattern period/4, and pattern period/2, respectively. Patterned incident photons are distributed randomly on the rectangular area of a pattern pitch (10 to 60 nm) by a 200 to 1000-nm length in the x and the y directions with irradiation dosage at around 20 $\mathrm{mJ/cm^2}$ (corresponding to 194 photons/$\mathrm{nm^2}$ for ArF or 13 photons/$\mathrm{nm^2}$ for EUV). For photons incident to a 20-nm-thick resist film, we count the numbers of various events such as elementary reactions in each voxel and calculate the histogram of various events per voxel for voxels under the same irradiation dose (with the same x coordinate). Probability density functions (PDF) are obtained as functions of image position x for various event numbers per voxel, such as photon absorption $\mathrm{pdf_{PA}}(x, n_{\mathrm{PA}})$, SE generation $\mathrm{pdf_{SE}}(x, n_{\mathrm{SE}})$, and elementary reaction $\mathrm{pdf_{ER}}(x, n_{\mathrm{ER}})$. For 1-D analysis, these PDFs are averaged in the z-direction, though this is a rough approximation for high absorption material. We assume that the voxel solubility flips when the elementary reaction number in a voxel exceeds a certain threshold nc_{ER}. The solubility of each voxel is determined with accounting for the intensity decay in the z direction. Then, we simply count the number

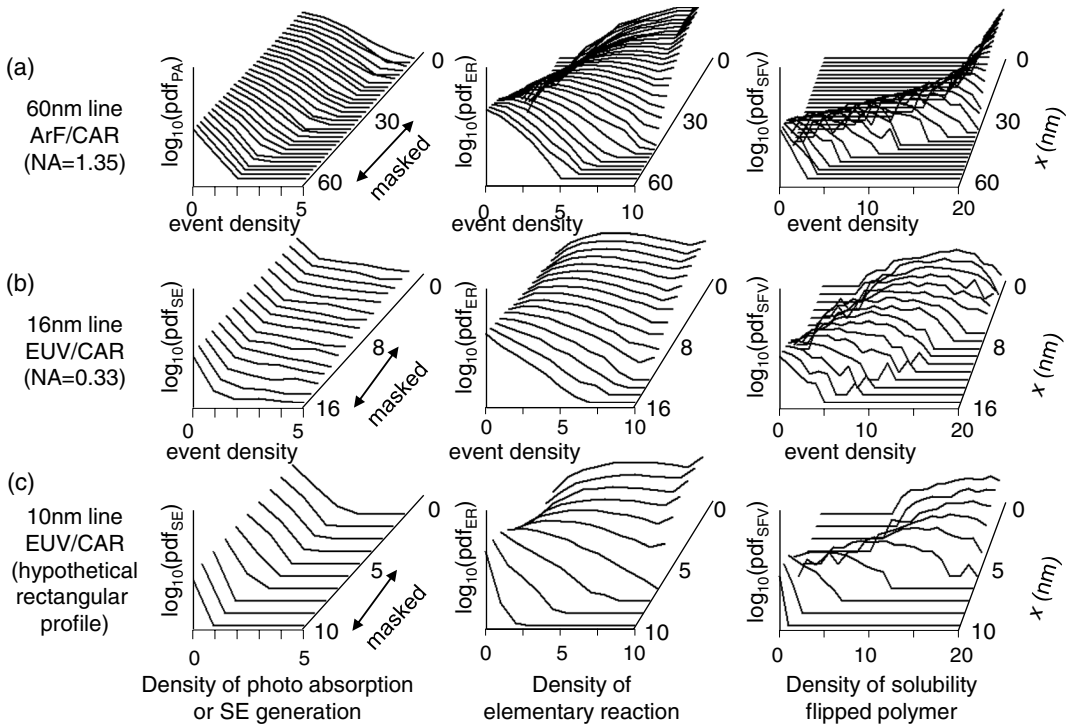

Fig. 2 PDF for various physical events (photon absorption, SE generation, elementary reaction, and voxel solubility flipping number through film thickness) as functions of image position x. Three typical optical systems are assumed, (a) 60-nm lines and spaces, ArF (193 nm), NA = 1.35, (b) 16-nm lines and spaces, EUV (13 nm), NA = 0.33, and (c) 10-nm lines and spaces, EUV, rectangular image profile (hypothetical). Only parts of PDFs higher than 0.001 are plotted.

n_{SFV} of solubility flipped voxels through film thickness at each horizontal position x and obtained their PDF, $\mathrm{pdf}_{\mathrm{SFV}}(x, n_{\mathrm{SFV}})$ as the measure of local film solubility.

Typical image position dependences of these PDFs are shown in Fig. 2 for three optical systems: (a) 60-nm line, ArF, NA = 1.35 (immersion lens), (b) 16-nm line, EUV, NA = 0.33, and (c) 10-nm line, EUV, hypothetical rectangular image profile. Since most of these distributions are difficult to fit into particular statistical models, we use original distributions in all the calculations in this study. Although differences between irradiated and masked regions is small in $\mathrm{pdf}_{\mathrm{PA}}(x, n_{\mathrm{PA}})$ and $\mathrm{pdf}_{\mathrm{SE}}(x, n_{\mathrm{SE}})$, the contrast between the two regions increases in $\mathrm{pdf}_{\mathrm{ER}}(x, n_{\mathrm{ER}})$ and $\mathrm{pdf}_{\mathrm{SFV}}(x, n_{\mathrm{SFV}})$. This is because homogenization through photoacid diffusion processes narrows dispersion of n_{ER}. However, the dispersion in $\mathrm{pdf}_{\mathrm{SFV}}(x, n_{\mathrm{SFV}})$ is wider in EUV than in ArF, meaning larger spatial nonuniformity in reaction density. Here, we point out larger inhomogeneity in SE generation observed in Fig. 1 as one of reasons for this. Even for the ideal rectangular image profile in Fig. 2(c), we observe similar dispersion in $\mathrm{pdf}_{\mathrm{ER}}(x, n_{\mathrm{ER}})$ and $\mathrm{pdf}_{\mathrm{SFV}}(x, n_{\mathrm{SFV}})$, and this directly represents nonuniformity in SE generation distribution.

3 Probabilistic Model of Pattern Defects

Next, we build probabilistic models for defect generations. We start from the definition of pattern formation and defect generation as follows; main patterns are formed if resist films remain in designated areas with designated thickness while they are completely removed for designated clear regions. In contrast, defects are defined as partially remained resist film in clear regions or as partial thickness loss in pattern regions, both resulting in undesired results after etching. The tolerable ratio of partially remaining or lost resist thickness to the designated thickness depends on etching processes.

Here, we assume negative-tone resist materials and they remain when insoluble voxels form 3-D networks connected to a substrate. We decompose this process into following two steps. First, for a local spot of film to be included in a network, it needs be insoluble. Assuming that a spot film is insoluble when the number n_{SFV} of solubility flipped voxel through film thickness is larger than a certain threshold nc_{SFV} film, the probability that the spot film is insoluble in the unit area at $x = x_i$ is

$$p_{\text{film solubility flip}}(x_i, nc_{\text{SFV film}}) = \int_{nc_{\text{SFV film}}}^{\infty} \mathrm{pdf}_{\mathrm{SFV}}(x_i, n_{\mathrm{SFV}})\mathrm{d}n_{\mathrm{SFV}}. \tag{1}$$

Here, note that nc_{SFV} is a process parameter while n_{SFV} is a probability variable.

Second, for the local spot to be connected to the main pattern network, the adjacent spot at $x = x_{i-1}$ needs to be a part of the network. Consequently, the probability that the local spot at $x = x_i$ becomes a part of main patterns is obtained by solving Eq. (2) for image position x:

$$P_{\text{main pattern}}(x_i) = P_{\text{main pattern}}(x_{i-1}) \cdot p_{\text{full film solubility flip}}(x_i). \tag{2}$$

For defect generation probability, we focus on bridge-type defects in negative-tone resists, undesirable formation of insoluble molecule/polymer network in clear regions. Here, we discuss two possible mechanisms separately; accidental series connections of shot noises across unexposed (clear) regions (mechanism A) and cascading SE generations along photoelectron trajectories traveling into unexposed (clear) regions from pattern regions (mechanism B). Note that the mechanism B exists only for EUV. Though these two mechanisms are not independent, full Monte Carlo simulation is necessary for dealing with the both comprehensively, and we separate them to use probability model approaches here.

For mechanism A, we treat each individual shot noise generation independently in accordance with the classical image of shot noise. This is similar to the case in previous main pattern formation, except that defect generation is limited within a certain height range of resist thickness, starting from pattern edges into clear regions. The probability that defect exists at $x = x_i$ when an edge is at $x = x_j (x_i > x_j)$ is expressed as

$$p_{\text{defect A}}(x_i|\text{edge} = x_j) = p_{\text{defect A}}(x_{i-1}|\text{edge} = x_j) \cdot p_{\text{partial film solubility flip}}(x_i) \cdot p_g. \quad (3)$$

Here, $p_{\text{Partial film solubility flip}}(x_i)$ is the probability that a part of film turns insoluble and is obtained by replacing $nc_{\text{SFV film}}$ of Eq. (1) to $nc_{\text{SFV defect}}$, and p_g is the geometrical factor representing the probability that neighboring insoluble voxels are within the height range connecting to neighboring defect network at $x = x_{i-1}$. As a boundary condition, $p_{\text{defect A}}(x_j|\text{edge} = x_j)$ is set to unity. The probability that defect exists at $x = x_i$ is obtained by integrating Eq. (4) for main pattern edge position as

$$P_{\text{defect A}}(x_i) = \int p_{\text{edge}}(x_j) \cdot p_{\text{defect A}}(x_i|\text{edge} = x_j)\mathrm{d}x_j. \quad (4)$$

In the analysis for mechanism A, we do not distinguish SEs in adjacent voxels are from different photoelectrons or from the same photoelectron and treat the probability that we find SE in each voxel independently. However, the probability that we find SEs in adjacent voxels is much higher if they are from the same photoelectron than they are from different photoelectrons, in particular when the photon absorption density is low. Thus, the analysis based on mechanism A underestimates the defect generation caused by SEs from an identical photoelectron, and we extract and evaluate such cases separately as mechanism B.

First, we calculate the probability of cascading SE generations since SE generations along photoelectron trajectory are in correlation. Here, an SE string is defined as a group of SEs generated along the same photoelectron trajectory with inter-SE distances shorter than a certain threshold (typically set to 1 nm in this study).

Defect probability in mechanism B is defined as the probability that the end of SE string reaches an evaluation point in the clear region center. To calculate this, we first calculate PDF, $p_{\text{SE string}}(x_i|\text{edge} = x_j, \text{photon} = r)$ that photoelectron emitted from $r = (x, y, z)$ generates an SE string between the main pattern edge at x_j and the evaluation point at x_i. We multiply this PDF with the probability that photon absorption exists at $r = (x, y, z)$, for which we can use the image intensity distribution $I(r)$. This gives us the probability that an SE string is generated between the edge at x_j and the position x_i when exposed with the image $I(r)$. Defect probability in mechanism B is obtained as the product summation of this and the edge distribution as

$$P_{\text{defect B}}(x_i) = \int P_{\text{edge}}(x_j) \cdot \{P_{\text{SE string}}(x_i|\text{edge} = x_j, \text{photon} = \vec{r}) \cdot I(\vec{r})\}\mathrm{d}x_j. \quad (5)$$

Typical examples of PDF of SE strings are shown in Fig. 3. From photoelectron scattering simulations, we first derive PDF for SE strings $\text{pdf}_{\text{SE string}}(\text{length}, \text{endpoint})$ with string lengths and their endpoint as probability variables

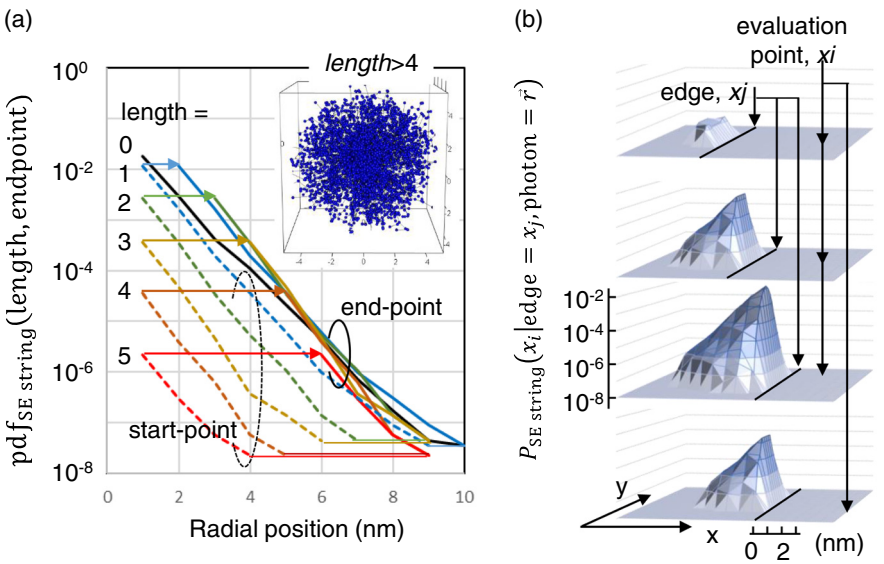

Fig. 3 Probability functions for SE strings. (a) $\text{pdf}_{\text{SE string}}(\text{length}, \text{endpoint})$ versus end point (solid lines) and start point (dashed lines), and (b) typical profiles of $p_{\text{SE string}}(x_i|\text{edge} = x_j, \text{photon} = r)$, both for SE energy = 10 eV, inter-SE distance = 2 nm.

[Fig. 3(a)]. Here, the string length is the value projected onto the direction of the endpoint from photon-absorption site. This PDF is further converted to PDF that photon absorption at $r_0 = (x_0, y_0, z_0)$ creates SE string from the main pattern edge position at $x = x_j$ to the defect evaluation position at $x = x_i$, $p_{\mathrm{SE\,string}}(x_i|\mathrm{edge} = x_j, \mathrm{photon} = r_0)$ [Fig. 3(b)]. Inset in Fig. 3(a) extracts SE strings longer than 4 nm out of 50k scattered photoelectrons.

4 Results and Discussions

Next, we calculate the probabilities of main pattern formation and defect generation using Eqs. (2), (4), and (5). Figure 4 shows typical probability profiles along the x axis with varying exposure dose. Here, we focus on CAR and assume optimized parameters discussed later. For ArF system [Fig. 4(a)], the defect generation probability (solid lines) decreases with the main pattern formation probability (broken line) outside pattern edge position, and the defect probability at the center of the clear region is negligibly small. In contrast, for EUV [Fig. 4(b)], the defect probability profiles extend into the clear region. Even in an ideal rectangular image profile, we observe significant defect probability in a clear region for mechanism B [Fig. 4(c)]. The higher mechanism A defect probability in EUV than in ArF reflects wider PDF distributions for the elementary reaction density in a clear region shown in Fig. 2, which is attributed to larger inhomogeneity in SE generations as explained in Fig. 1. For EUV, the mean feature sizes of delineated pattern and corresponding defect probabilities at the clear region center are obtained from main-pattern and defect probability profiles for each parameter set. Here, we calculated the mean feature size from averaging edge position probability distribution obtained as $P_{\mathrm{main\ pattern}}(x - \delta x)\,[1 - P_{\mathrm{main\ pattern}}(x + \delta x)]$. To minimize defect probabilities with keeping the delineated features size at around designated size, we applied multiobjective genetic algorithm with setting the discrepancy between delineated and design sizes and the probabilities of defect due to mechanisms A and B as objective functions.[20] Physical and chemical parameters required in the above calculations are not always clear, and we assume the following parameter ranges for control variables: irradiation dose (20 to 40 mJ/cm^2), resist photon absorption (0.001 to 0.02 nm^{-1}), acid diffusion length (2 to 4 nm), catalytic chain length (10 to 40), and number of elementary reaction required for voxel solubility flipping (4 to 8/nm^3). SE energy per inelastic scattering (10 to 20 eV or PE energy$^{0.5}$), elementary reaction site density (10/nm^3), voxel size (1 nm), and the number of solubility flipped voxels through film thickness nc_{SFV} required for generating main pattern (10) and film defect (3) are set constant during the optimization. Note that the above parameter ranges are for examining basic behaviors of the model and do not reflect any practical materials.

Typical optimization results (eight generations of 64 populations) are shown in Fig. 5 (black dots) for each defect mechanism. Each point in the figures corresponds to a particular parameter set, and distributions of performance show a tradeoff relationship between the clear region width and defect probabilities. The lower limit of the distribution shows the Pareto solution and performance better than this limit is difficult within the assumed parameter space. When changing exposure dose only, we observed the defect probability exponentially increases with decreasing the delineated clear region width, and this agrees with experimental results.[1] This exponential relationship is not scaled with resolution capability of imaging system but depends on the absolute size (clear region width) of delineated pattern, resulting in higher defect probabilities for smaller target size [Fig. 5(a), red squares]. Even for the ideal rectangular image profile, significant defect probabilities are predicted for the mechanism B [Fig. 5(a), blue crosses].

The exponential dependence of defect probabilities on the pattern size is explained as follows. In the mechanism A, the defect probability is the direct product of spot film defect probabilities (per unit area) between the edge and clear region center. In mechanism B, it is the probability that photoelectrons travel from the pattern edge to the clear region center. In both cases, it exponentially decreases with increasing the distance from the pattern edge to the clear region center. The contributions from the two mechanisms are roughly comparable although the absolute comparison between them is difficult because the defect generation criteria are different between the two.

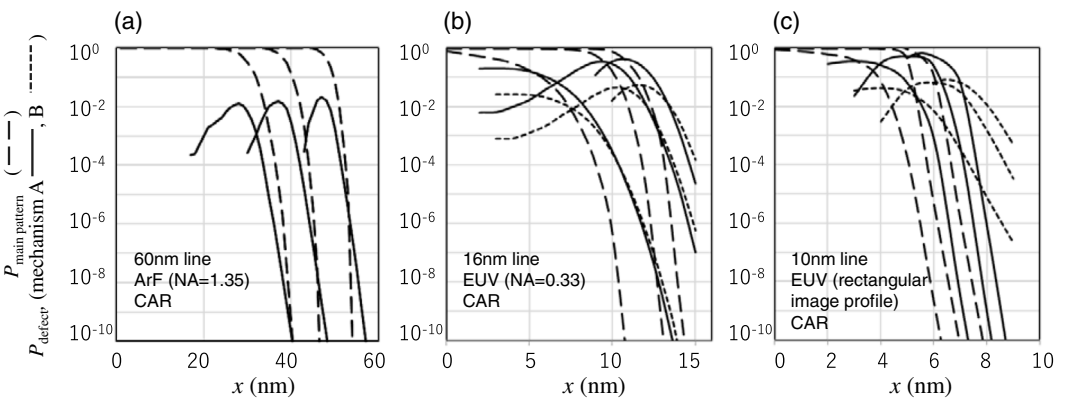

Fig. 4 Probabilities of defect generation (mechanism A: solid lines, mechanism B: dotted lines) and main pattern formation (broken lines) along the x-axis with varying exposure dose (15 to 40 mJ/cm^2). Typical material parameter sets are assumed for each case. (a) 60-nm lines and spaces by ArF (NA = 1.35)/CAR, (b) 16-nm lines and spaces by EUV (NA = 0.33)/CAR, and (c) 10-nm lines and spaces by EUV (hypothetical rectangular image profile)/CAR.

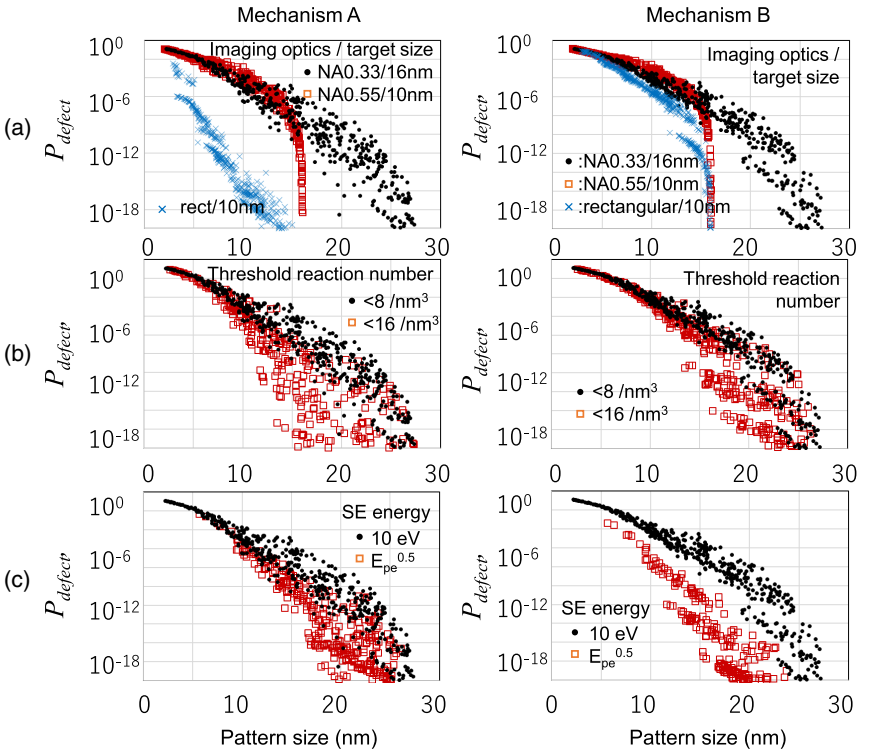

Fig. 5 Distributions of defect probabilities and delineated pattern sizes as results of the optimization processes using multiobjective genetic algorithm. (a) Dependences on design size and imaging systems, (b) dependences on reaction site density and solubility flipping threshold, and (c) dependences on SE energy assumption.

Finally, we suggest some directions for stochastic defects suppression. Defect generation in mechanism A is due to inhomogeneity in elementary reaction density in the clear region. Increasing photon absorption density or enhancing acid catalysis reduces this but changes delineated pattern sizes. To solve this dilemma, we suggest increasing the reaction site density and the upper limit of the film solubility flipping threshold. The evolution of control parameters during optimization also supported this, and optimization with increasing the upper limit for the range of elementary reaction number required for voxel solubility flipping shows reduction in the mechanism A defect probabilities [Fig. 5(b), red squares]. For mechanism B defect, optimization results with changing the assumption of Ese (from 10 eV to square root of photoelectron energy) show a reduction in the defect probabilities [Fig. 5(c), red squares]. Although photoelectron scattering parameters inside resists are unclear, introducing material compositions with increased elastic and inelastic scattering cross-sections narrows the dispersion of $\mathrm{pdf}_{\mathrm{SE\,string}}(\mathrm{length}, \mathrm{endpoint})$ and suppresses the mechanism B. Defect probabilities depend also on main-pattern edge distribution because they exponentially decrease with increasing the distance from edges. Thus, low LER patterning conditions are effective, although this is often equivalent to the above two guidelines.

Though in-detailed parameter optimization is beyond the scope of this paper, our results showed basic behaviors of stochastic defects in EUV lithography. Interesting question where the present material systems located in the parameter space is open.

5 Appendix: Coupled Monte Carlo Simulation

5.1 *Calculation of Photon Absorption Event Locations*

The locations (x_i, y_i) of incident photons on a resist film surface through a mask are extracted from locations randomly distributed with given area density in $L_x \times L_y$ area by accepting (x_i, y_i) if $R1_i < \mathrm{image}(x_i, y_i)$ using Von Neumann's rejection sampling method. (R represents random value uniformly distributed in [0,1] segment.) We calculate normalized intensity distribution $\mathrm{Image}(x, y)$ by the partial coherent theory as

$$\mathrm{Image}(x,y)=\sum_s \{F[\mathrm{MASK}(X-X_s,Y-Y_s)\cdot\mathrm{PUPIL}(X,Y)]\}^2,$$

where $\mathrm{MASK}(X, Y)$ is Fourier transform F of a mask transmission function, $\mathrm{mask}(x, y)$, X_s, Y_s $(s = 1, .., n_s)$ are illumination source locations, and $\mathrm{PUPIL}(X, Y)$ is a pupil function. For a photon incident to the resist film at (x_i, y_i), we generate photon absorption at depth z_i as

$$z_i = -\alpha \ln(1 - R2_i).$$

5.2 *Calculation of Electron Scattering Event Locations*

For a photoelectron generated at $r_0 = (0,0,0)$, the locations of inelastic scattering events $\delta r_j = (\delta x_j, \delta y_j, \delta z_j)$ are calculated as follows:

$$L = \lambda_{\text{total}} \cdot \ln(1 - R3_j), \quad \frac{1}{\lambda_{\text{total}}} = \frac{1}{\lambda_{\text{elastic}}(E_{\text{PE}})} + \frac{1}{\lambda_{\text{inelastic}}(E_{\text{PE}})},$$

$$\delta r_n = \begin{cases} \delta r_{n-1} + s_n \cdot L_n, & \left(\text{if } R4_n < \frac{\lambda_{\text{total}}}{\lambda_{\text{elastic}}(E_{\text{PE}n-1})}, \text{elastic scattering}\right) \\ \delta r_{n-1} + s_{n-1} \cdot L_n, & \left(\text{if } R4_n \geq \frac{\lambda_{\text{total}}}{\lambda_{\text{elastic}}(E_{\text{PE}n-1})}, \text{inelastic scattering}\right) \end{cases},$$

$$E_{\text{PE}n} = E_{\text{PE}n-1} - E_{\text{SE}} \quad \left(\text{if } R4_n \geq \frac{\lambda_{\text{total}}}{\lambda_{\text{elastic}}(E_{\text{PE}n-1})}, \text{inelastic scattering}\right).$$

Here, E_{PE} and E_{SE} are energies of photoelectron and SE. λ_{elastic} and $s_n = [a_n(E_{\text{PE}}), b_n(E_{\text{PE}}), c_n(E_{\text{PE}})]$ are calculated from Mott cross-section [21] and semiempirical relation[12] is used for calculating $\lambda_{\text{inelastic}}$. Inelastic scattering events are extracted from the above sequence of scattering events and are renumbered.

5.3 *Calculation of Acid Catalytic Reaction Event Locations*

For a photoacid generated at $r_0 = (0,0,0)$, the locations of potential catalytic reaction δr_k = (δx_k, δy_k, and δz_k) are extracted from locations randomly distributed with given reaction site density by accepting δr_k if $R5_k < P_{\text{acid}}(\delta r_k, D_{\text{diff}})$ using Von Neumann's rejection sampling method. We approximate the acid existence probability P_{acid} (r, D_{diff}) by Gaussian distribution with a blur D_{diff}. N_{ccl} (catalytic chain length) points are randomly selected from the above extracted potential catalytic reaction location as acid catalytic reaction event locations.

The final catalytic reaction location $r_l = (x_l, y_l, z_l)$ through resist film are obtained as

$$r_l = r_i + \delta r_{ij} + \delta r_{ijk},$$

where δr_{ij} is the location of the j'th photoacid (or SE) generation along the photoelectron trajectory from the i'th photoabsorption event, and δr_{ijk} is the location of the k'th reaction induced by the j'th photoacid from the i'th photoabsorption. These locations are calculated for every photons, SEs, and reactions in the resist film independently.

Acknowledgments

H.F. wishes to thank M. Suzuki for support in electron scattering simulation.

References

1. P. De Bisschop, "Stochastic effects in EUV lithography: random, local CD variability, and printing failures," *J. Micro/Nanolithogr. MEMS MOEMS* **16**(4), 041013 (2017).
2. R. van Es et al., "EUV for HVM: towards and industrialized scanner for HVM NXE3400B performance update," *Proc. SPIE* **10583**, 105830H (2018).
3. P. Naulleau, S. Bhattarai, and A. Neureuther, "Understanding extreme stochastic events in EUV resists," *J. Photopolym. Sci. Technol.* **30**, 695–701 (2017).
4. A. Yamaguchi et al., "Characterization of line-edge roughness in resist patterns and estimations of its effect on device performance," *Proc. SPIE* **5038**, 689–698 (2003).
5. H. Fukuda, "Analysis of line edge roughness using probability process model for chemically amplified resists," *Jpn. J. Appl. Phys.* **42**(6B), 3748–3754 (2003).
6. F. Wang et al., "Assessment of variability and defectivity by high-throughput e-beam metrology for prediction of patterning defect probabilities," *Proc. SPIE* **10585**, 1058525 (2018).
7. R. Brainard et al., "Shot noise, LER and quantum efficiency of EUV photoresists," *Proc. SPIE* **5874**, 74–85 (2004).
8. A. Narasimhan et al., "Studying secondary electron behavior in EUV resists using experimentation and modeling," *Proc. SPIE* **9422**, 942208 (2015).
9. A. V. Pret et al., "Modeling and simulation of low-energy electron scattering in organic and inorganic EUV photoresists," *Proc. SPIE* **10146**, 1014609 (2017).
10. W. G. Oldham et al., "A general simulator for VLSI lithography and etching processes: part I-application to projection lithography," *IEEE Trans. Electron Devices* **26** (4), 717–722 (1979).
11. R. Shimizu et al., "A Monte Carlo approach to the direct simulation of electron penetration in solids," *J. Phys. D: Appl. Phys.* **9**, 101–113 (1976).
12. M. P. Seah and W. A. Dench, "Quantitative electron spectroscopy of surfaces: a standard data base for electron inelastic mean free paths in solids," *Surf. Interface Anal.* **1**(1), 2–11 (1979).
13. H. Ito, "Chemical amplification resists for microlithography," *Adv. Polym. Sci.* **172**, 37–245 (2005).
14. T. Kozawa and S. Tagawa, "Radiation chemistry in chemically amplified resists," *Jpn. J. Appl. Phys.* **49**(3), 030001 (2010).
15. D. De Simone et al., "EUV photoresist patterning characterization for IMEC N7/N5 technology," *Proc. SPIE* **10583**, 105830G (2018).
16. Z. Tasdemir et al., "Chemically-amplified EUV resists approaching 11 nm half-pitch," *Proc. SPIE* **10583**, 105831W (2018).
17. S. Grzeskowiak et al., "Electron trapping: a mechanism for acid production in extreme ultraviolet photoresists," *J. Micro/Nanolithogr. MEMS MOEMS* **17**, 033501 (2018).
18. A. Grenville et al., "Integrated FAB process for metal oxide EUV photoresist," *Proc. SPIE* **9425**, 94250S (2015).
19. P.-J. Wu et al., "Nanoscale inhomogeneity and photoacid generation dynamics in extreme," *Proc. SPIE* **10586**, 105861O (2018).
20. K. Deb, A. Pratap, and S. Agarwal, "A fast and elitist multiobjective genetic algorithm: NSGAII," *IEEE Trans. Evol. Comput.* **6**(8), 182–197 (2002).
21. D. C. Joy, *Monte Carlo Modeling for Electron Microscopy and Microanalysis*, Oxford University Press, New York (1995).

Hiroshi Fukuda joined Hitachi Central Research Laboratory in 1985, where he has engaged in various fields of lithography as well as nanodevices, MEMS, and HDD, including research activities in Stanford university and Hitachi Europe Ltd. He has been with Hitachi High-technologies since 2012. He received his BS, MS and PhD degrees from Tokyo Institute of Technology in 1983, 1985, and 1994, respectively. He has published more than 30/80 journal/conference papers and holds over 20 patents.